



# Atomic layers of ruthenium oxide coupled with Mo<sub>2</sub>TiC<sub>2</sub>T<sub>x</sub> MXene for exceptionally high catalytic activity toward water oxidation

Jitendra N. Tiwari<sup>a,\*</sup>, Muhammad Umer<sup>b</sup>, Gokul Bhaskaran<sup>c</sup>, Sohaib Umer<sup>b</sup>, Geunsik Lee<sup>b</sup>, Min Gyu Kim<sup>d</sup>, Han-Koo Lee<sup>e</sup>, Krishan Kumar<sup>c</sup>, A.T. Ezhil Vilian<sup>a</sup>, Yun Suk Huh<sup>c,\*</sup>, Young-Kyu Han<sup>a,\*</sup>

<sup>a</sup> Department of Energy and Materials Engineering, Dongguk University-Seoul, Seoul 100-715, Republic of Korea

<sup>b</sup> Center for Superfunctional Materials, Department of Chemistry, Ulsan National Institute of Science and Technology (UNIST), 50 UNIST-gil, Ulsan 44919, Republic of Korea

<sup>c</sup> Department of Biological Sciences and Bioengineering, Nano Bio High-Tech Materials Research Center, Inha University, Incheon 22212, Republic of Korea

<sup>d</sup> Beamline Research Division Pohang Accelerator Laboratory (PAL), Pohang 37673, Republic of Korea

<sup>e</sup> Pohang Accelerator Laboratory, POSTECH, Pohang 790-784, Republic of Korea

## ARTICLE INFO

### Keywords:

Mo<sub>2</sub>TiC<sub>2</sub>T<sub>x</sub> MXene  
Ruthenium oxide  
Density functional theory  
Molecular dynamics (MD) simulations  
Oxygen evolution reaction  
Water splitting

## ABSTRACT

Progress in acidic water splitting has remained limited because of low oxygen evolution reaction (OER) activities, sluggish reaction kinetics, and severe catalyst degradation. Thus, a highly active and durable OER catalyst is required for the commercialization of acidic water electrolyzers. Here, we report *t*-phase ruthenium oxide atomic layers implanted on Mo<sub>2</sub>TiC<sub>2</sub>T<sub>x</sub> MXene (**R<sub>AL</sub>-M**) as a model electrocatalyst for the OER in acidic media, which exhibits a remarkable mass activity (6.2 A mg<sup>-1</sup>), excellent turnover frequency (TOF; 2.4 s<sup>-1</sup>), and negligible loss of durability after 22 h in a two-electrode cell configuration. The mass activity and TOF of **R<sub>AL</sub>-M** are 150 times (RuO<sub>2</sub>-Premetek Co.) and 540 times (RuO<sub>2</sub>-Sigma-Aldrich) greater than the industrially adopted electrocatalysts at pH 0.48. Computational calculations show that the ruthenium active sites of **R<sub>AL</sub>-M** have a strong affinity to oxygen species (e.g., OH\*, O\*, and OOH\*), which efficiently adapts water dissociation and favors both the adsorbate evolution and lattice oxygen mechanistic pathways to accelerate the OER.

## 1. Introduction

Chemical energy storage is one of the best ways to address global energy consumption and climate challenges.[1–5] The oxygen/hydrogen evolution reaction (OER/HER) plays an important role in grid-scale energy storage.[6] Considering the cathodic electrode of acidic water splitting (referred to as HER), platinum-based materials are ideal electrocatalysts for the reduction of water to molecular hydrogen.[7] However, active, stable, and cheap electrocatalysts are required for the anodic electrode (oxidation of water to molecular oxygen in a strongly acidic environment, referred to as OER).[8,9] The OER in acidic electrolytes can proceed via the adsorbate evolution mechanism (AEM) or the lattice-oxygen mechanism (LOM).[10,11] The OER is a very sluggish half-reaction process owing to the multi-proton/electron-coupled kinetics.[12,13] Therefore, it plays an important role in the overall efficiency of electrically driven water splitting. Iridic oxide is currently the most frequently used but an

expensive catalyst to drive the OER, especially for industrial acidic water electrolyzers based on polymeric membranes.[14–16] However, the scarcity of this metal, high overpotential, and instability in acidic environments hinder their widespread adoption.[17] Therefore, developing alternative electrocatalysts with reduced precious metal loading is a challenge. In this regard, we first investigated acid-stable substrate materials because graphene-like materials [18] degrade because of carbon corrosion at high oxidative potentials.[19,20] MXenes[21] (specifically for dual-transition metals) are promising alternatives as they are prepared in harsh acidic environments[22] and are extremely stable in deionized (DI) water at room temperature (Fig. S1). Secondly, ruthenium oxide (RuO<sub>2</sub>) shows high reactivity to the OER owing to its ideal capacity to attach oxygen during acidic water oxidation.[23] The price of ruthenium (21 €/g) is ~8 times cheaper than that of iridium (168 €/g).[24] Single atoms and monatomic layers are used to reduce the metal amount on the surface of substrate materials and improve their mass activity.[25–34] However, due to the presence of single-atom

\* Corresponding authors.

E-mail addresses: [jnt.tiw123@yahoo.co.in](mailto:jnt.tiw123@yahoo.co.in) (J.N. Tiwari), [yunsuk.huh@inha.ac.kr](mailto:yunsuk.huh@inha.ac.kr) (Y.S. Huh), [ykenenergy@dongguk.edu](mailto:ykenenergy@dongguk.edu) (Y.-K. Han).

<https://doi.org/10.1016/j.apcatb.2023.123139>

Received 25 March 2023; Received in revised form 10 June 2023; Accepted 28 July 2023

Available online 29 July 2023

0926-3373/© 2023 Elsevier B.V. All rights reserved.

catalytic sites, single-metal atoms are not sufficiently active in four-electron reactions, such as the OER[35] and the oxygen reduction reaction.[36] In the case of atomic layers, the involvement of a large number of accessible active sites facilitates four-electron process reactions.[37–43] Therefore, the synthesis of the monatomic layer or sheet of *t*-phase RuO<sub>2</sub> (*t*-RuO<sub>2</sub>) on MXene not only decreases the catalyst cost by reducing Ru loading but also dramatically increases the mass activity.

Based on these considerations, we report a distorted *t*-RuO<sub>2</sub> atomic layer (**R<sub>AL</sub>**) on the Mo<sub>2</sub>TiC<sub>2</sub>T<sub>x</sub> MXene (**M**) surface (hereafter abbreviated as **R<sub>AL</sub>-M**). The amount of Ru on the **M** substrate is 1.76 wt%, which is 43 times smaller than that of commercial RuO<sub>2</sub> (75.95 wt%; Premetek Co. and Sigma-Aldrich) catalysts (Table S1). **R<sub>AL</sub>-M** exhibited remarkable OER activity evidenced by ultrahigh mass activity and excellent stability, which outperforms the state-of-the-art catalysts and surpasses previously reported activities (Table S2). First-principles calculations reveal that the high density of active sites and the synergistic interactions between **R<sub>AL</sub>** and **M** tune the Ru *d*-band electronic density of states near the Fermi level, which lowers the energy barrier for water dissociation and thus facilitates water adsorption. Meanwhile, the strong electronic interactions between high-valence Mo ions (Mo<sup>4+</sup>, Mo<sup>5+</sup>, Mo<sup>6+</sup>, and Ti<sup>4+</sup>) and **R<sub>AL</sub>** (Ru<sup>>4+</sup>) result in a more stable surface structure during the OER process, confirming the excellent stability of **R<sub>AL</sub>-M**. The computationally predicted overpotential trends (implicit and explicit solvent models) in acidic water splitting agree well with the experimental results.

## 2. Experimental section

### 2.1. Materials and chemicals

Molybdenum titanium aluminum carbide (Mo<sub>2</sub>TiAlC<sub>2</sub>) MAX phase powder (500 mesh) was purchased from Angong Niu Huang Wan. EG (CAS # 107–21–1) and hydrochloric acid (CAS # 7647–01–0) were purchased from Daejung. Hydrofluoric acid (CAS # 7664–39–3; ≥48%), ruthenium (III) chloride hydrate (CAS # 14898–67–0), ruthenium (IV) oxide (CAS # 12036–10–1; 99.9%), perchloric acid (CAS # 7601–90–3; 70%), and sulfuric acid (CAS # 7664–93–9; 99.999%) were purchased from Sigma-Aldrich. Ruthenium (IV) oxide (Item # P20V020) was purchased from Premetek Co. All chemicals were of analytical grade and used without further purification.

### 2.2. Preparation of Mo<sub>2</sub>TiC<sub>2</sub>T<sub>x</sub> MXene (**M**)

An exfoliation approach was used to prepare Mo<sub>2</sub>TiC<sub>2</sub>T<sub>x</sub> MXene (**M**) from Mo<sub>2</sub>TiAlC<sub>2</sub> MAX phase powder by the selective etching of Al. In a typical process, 1 g Mo<sub>2</sub>TiAlC<sub>2</sub> MAX powder was mixed with 40 ml of the etchant (20 ml HF and 20 ml HCl). The MAX powder was poured slowly to avoid overheating due to the exothermic reaction. The etching process was conducted in Teflon vessels for 6 days in a water bath at 60 °C. Then, the slurry was divided into two parts and poured into two vessels. Next, 30 ml of HF and 30 ml of HCl were added to each of the two vessels and stirred at room temperature for 12 h. The obtained slurry was separated by centrifugation and washed eight times with DI water (Milli-Q water, 18.2 MΩ cm). The wet product was then redispersed in 1 L of DI water and exfoliated by ultrasonication for 1 h. After ultrasonication, the solution was left overnight, and the few layers of **M** were maintained in a suspended state, while multilayers of **M** settled rapidly. The supernatant was collected by centrifugation and then freeze-dried for 3 days to obtain the powder of few-layers **M**.

### 2.3. Synthesis of **R<sub>AL</sub>-M**

At first, 70 mg of ruthenium (III) chloride hydrate and 30 mg of **M** powder were dispersed for 2 h in 35 and 30 ml of EG, respectively. Then, the two solutions were slowly mixed and stirred for 12 h. Next, the mixture was injected into a conical flask (Borosilicate glass; 250 ml). The flask was then placed in microwave oven (LG Electronics MR-M201, see

Fig. S2) operating at the power of 620 W and heated for 3 min. After cooling to room temperature, the solution was centrifuged and washed several times with DI water (4 times) and ethanol (2 times). The slurry was poured into a glass Petri dish and dried at room temperature. The product was finally heated in a muffle furnace at 350 °C (temperature rise rate of 35 °C/min) in air for 15 min to generate a distorted **R<sub>AL</sub>** on the **M** surface. The prepared catalyst was labeled as **R<sub>AL</sub>-M** and directly used for electrochemical testing.

### 2.4. Synthesis of **R<sub>AL</sub>**

The whole procedure was the same as that of **R<sub>AL</sub>-M**, except for the use of **M**. The obtained sample was labeled as **R<sub>AL</sub>**.

### 2.5. Synthesis of **R<sub>AL</sub>-M<sub>1</sub>**

The entire procedure was similar to that of **R<sub>AL</sub>-M**, except for the use of an oxidation temperature of 300 °C. The obtained sample was labeled as **R<sub>AL</sub>-M<sub>1</sub>**.

### 2.6. Synthesis of **R<sub>AL</sub>-M<sub>2</sub>**

The entire procedure was similar to that of **R<sub>AL</sub>-M<sub>1</sub>**, except for the use of an oxidation temperature of 400 °C. The obtained sample was labeled as **R<sub>AL</sub>-M<sub>2</sub>**.

### 2.7. Synthesis of **R<sub>AL</sub>-M<sub>3</sub>**

The entire procedure was similar to that of **R<sub>AL</sub>-M**, except for the use of a duration of 10 min. The obtained sample was labeled as **R<sub>AL</sub>-M<sub>3</sub>**.

### 2.8. Synthesis of **R<sub>AL</sub>-M<sub>4</sub>**

The entire procedure was similar to that of **R<sub>AL</sub>-M**, except for the use of a duration of 20 min. The obtained sample was labeled as **R<sub>AL</sub>-M<sub>4</sub>**.

### 2.9. Synthesis of **R<sub>AL</sub>-M<sub>5</sub>**

The whole procedure was the same as that of **R<sub>AL</sub>-M**, except for the use of thermal oxidation. The obtained sample was labeled as **R<sub>AL</sub>-M<sub>5</sub>**.

### 2.10. Synthesis of **R<sub>AL</sub>-C** (RuO<sub>2</sub>-C)

In a typical process, 70 mg of ruthenium (III) chloride hydrate and 60 mg of carbon powder (C, Vulcan XC72R) were dispersed for 2 h in 35 and 30 ml of EG, respectively. Then, the two solutions were slowly mixed and stirred for 12 h. Next, the solution was heated in a microwave oven for 3 min. After cooling to room temperature, the solution was centrifuged and washed several times with DI water and ethanol. The slurry was poured into a glass Petri dish and dried at room temperature. The product was finally heated in a muffle furnace at 350 °C (temperature rise rate of 35 °C/min) in the air for 15 min to deposit a **R<sub>AL</sub>** on the carbon black. The prepared catalyst was labeled as **R<sub>AL</sub>-C**. The amount of Ru in **R<sub>AL</sub>-C** is 25.5 wt% as determined by thermogravimetric analysis (TGA; Fig. S3). Accordingly, the Ru amount is:

$$75.95 \times 33.53/100 = 25.5 \text{ wt\%}.$$

### 2.11. Characterization of electrocatalysts

The thickness of exfoliated **M** sheets was obtained via atomic force microscopy (Multimode IVa). The surface morphology of the electrocatalysts was characterized using an SU 8010 (Hitachi Ltd., Japan) scanning electron microscope (SEM) operated at 15.0 kV. The microstructure, lattice structures, and element distribution of electrocatalysts were investigated by field-emission TEM and high-resolution TEM (HRTEM; JEOL JEM-2100 F; operated at an accelerating voltage of 200

kV). The element distribution was conducted by a JEM-2100 F transmission electron microscope. The amount of Ru content was directly assessed by inductively coupled plasma optical emission spectrometry (ICP-OES; Optima 7300 DV, PerkinElmer, USA). The elemental composition and chemical valence states were obtained by XPS; Thermo Scientific K-Alpha; Al K $\alpha$  probe beam; spot size 3–4  $\mu\text{m}$ ; ion source energy 100 V–3 kV). XPS spectra were calibrated using C 1 s at 284.6 eV. Powder X-ray diffraction (XRD) was carried out on a PANalytical X'Pert (Pro MRD) diffractometer with Cu K $\alpha$  radiation ( $\lambda = 1.5406 \text{ \AA}$ ). NEXAFS measurements for O K-edge were performed at the 10A2 beamline of the Pohang Accelerator Laboratory (PAL). X-ray absorption spectra were recorded for analyzing the chemical state of the electrocatalyst at the 10 C beamline of the PAL (10 C-wide EXAFS), Pohang, Republic of Korea. Background removal, normalization, and FT were performed by the ATHENA program. The extracted EXAFS signal  $\chi(r)$  and  $k^3\chi(k)$  were plotted for all metals. The Artemis program was employed for EXAFS fitting.

## 2.12. Electrochemical measurements

A standard three-electrode system (electrochemical analyzer/workstation, CH Instruments, Inc; CHI7045E, Austin, TX, USA) consisting of a working electrode, a reference electrode (Ag/AgCl electrode; saturated 3.0 M KCl solution), and a counter electrode (graphite rod;  $\Phi 10 \times 100 \text{ mm}$ ) was employed to assess the OER activities of all electrocatalysts in an O<sub>2</sub>-saturated 0.5 M H<sub>2</sub>SO<sub>4</sub>/0.5 M HClO<sub>4</sub> electrolytes at 25 °C. The electrolytes were pre-purged with oxygen gas for at least 20 min prior to OER measurements. The glassy carbon electrode (GCE, 5 mm inner diameter, 0.196 cm<sup>2</sup>) and graphite sheets with a size of 1 × 2 cm<sup>2</sup> were used as the working electrode, respectively. The homogeneous catalyst ink was made by ultrasonically dispersing a mixture containing 5 mg of the catalyst, 0.5 mg of carbon black Super-P (conductive agent), 0.39 ml of isopropyl alcohol, 0.6 ml of DI water (18.2 M $\Omega$  cm), and 10  $\mu\text{L}$  of Nafion (5 wt%). Then, 15  $\mu\text{L}$  and 76.55  $\mu\text{L}$  of the homogeneous inks were pipetted out and dropped onto the pre-cleaned GCE and graphite sheets and then completely dried at room temperature. For comparison, commercial RuO<sub>2</sub> catalysts (Premetek Co., Sigma-Aldrich) supported on the GCE and graphite sheets were also obtained by the drop-casting method. To stabilize the working electrodes, several cyclic voltammetry (CV) scans were conducted at a scan rate of 50 mV s<sup>-1</sup> in the potential range of 1.0–1.4 V versus RHE. The anodic linear sweep voltammograms were collected at a scan rate of 2 mV s<sup>-1</sup>. The stability tests were conducted on both three- and two-electrode cells. In a three-electrode cell, chronoamperometry (CA) responses were recorded on graphite sheets at potentials attaining a current density of 10 mA cm<sup>-2</sup>. Polarization curves measured before and after the stability (CA) tests were collected for comparison. With and without the membrane-separated two-electrode cell, chronopotentiometry (CP) responses were recorded on graphite sheets (the catalyst loading was 5 mg cm<sup>-2</sup>) as the current densities reached 10 mA cm<sup>-2</sup>. The LSV, CA, and CP curves were plotted with 100% *iR*-compensation. To ensure repeatability, all reported measurements were repeated at least three times. The EIS was tested on the GCE by AC impedance spectroscopy at different potentials (V versus RHE) in a frequency range of 10<sup>5</sup>–0.1 Hz with an amplitude of 5 mV in a 0.5 M H<sub>2</sub>SO<sub>4</sub> electrolyte. All potentials were transformed to RHE according to the reference electrode calibration value (Fig. S4).

The Tafel slopes were calculated using the following formula:

$$\eta = b \log j + c$$

where  $\eta$  is the overpotential,  $j$  is the current density,  $b$  is the Tafel slope, and  $c$  is the intercept.

The overpotential was assessed using the following formula:

$$\eta = E \text{ (versus RHE)} - 1.23 \text{ V}$$

### 2.12.1. Electrochemically active surface area (ECSA) calculation

The ECSAs of all samples were determined from the double-layer capacitance ( $C_{dl}$ ) of the electrocatalyst surface.  $C_{dl}$  was calculated in a non-Faradic region (1.15–1.35 V versus RHE) associated with double-layer charging from the sweep rate dependence of CV. Various sweep rates (10, 20, 30, 40, 50, 60, 70, 80, 90, and 100 mV s<sup>-1</sup>) were applied to conduct CV scans. The current ( $\Delta i/2 = (i_a - i_c)/2$ ) calculated at a fixed potential of 1.25 V (versus RHE) from the CV curves is linearly related to the sweep rate, and the slope achieved from the linear fitting of the current and the scan rate was considered to be  $C_{dl}$ . The ECSAs of the electrocatalysts were estimated from  $C_{dl}$  according to the following formula:

$$\text{ECSA} = C_{dl}/C_s$$

where the specific capacitance ( $C_s$ ) is 0.035 mF cm<sup>-2</sup> in H<sub>2</sub>SO<sub>4</sub>.

## 2.13. Computational details

Spin-polarized DFT calculations were conducted using the Vienna ab initio simulation package (VASP).[44] The ion–electron interaction was described by employing projector augmented wave pseudopotentials. The exchange-correlation energy functional was described by the Perdew–Burke–Ernzerhof (PBE) functional[45,46] generalized gradient approximation. The valence orbitals were described by plane-wave basis sets with a kinetic cutoff energy of 500 eV. The  $\Gamma$ -centered k-points in the Brillouin zone were sampled by an 11 × 11 × 1 grid to relax the unit cells and a 7 × 7 × 1 k-points grid for the optimization of the 4 × 4 × 1 supercell. The proposed models for **R<sub>AL</sub>**, **M** (Mo<sub>2</sub>TiC<sub>2</sub>O<sub>2</sub>), **R<sub>AL</sub>-M**, and a five-layer 2 × 4 × 2 supercell size RuO<sub>2</sub> (110) surface are shown in Fig. S5, and possible reaction pathways are depicted in Fig. 5a. The vacuum space of 20 Å in the z-direction was added to avoid artificial interactions between periodic images. In addition, the Tkatchenko–Scheffler (TS) method was used with standard parameters to describe the van der Waals (vdW) interactions between adsorbed species and the catalyst.[47] The solvation effect was taken into account using the pure implicit solvent model as implemented in VASPsol.[48] All structures were fully optimized until the energy difference between two consecutive iterations and residual force on each atom were less than 1.0 × 10<sup>-5</sup> eV and 0.01 eV Å<sup>-1</sup>, respectively. The ab initio molecular dynamics (AIMD) simulations were performed at 500 K by using the Nose-Hoover thermostat method (see Supplementary material for details) [49].

## 3. Results and discussion

### 3.1. Electrocatalyst synthesis and general characterization

The **R<sub>AL</sub>-M** electrocatalyst was prepared using three main steps (Fig. 1a, see Experimental section). In the first step, delaminated **M** layers were fabricated by the selective etching of Mo<sub>2</sub>TiAlC<sub>2</sub> MAX powder, followed by subsequent sonication-assisted exfoliation and freeze-drying. The atomic force microscopy image shows a typical 2D morphology with increasing thickness from 1.7 to 4.2 nm (i.e., 2–4 **M** layers) (Fig. S6, Note S1). During the etching process, many hydrophilic functional groups (such as –OH and =O) were present on the surface of **M** (Fig. S7). In the second step, exfoliated **M** layers and Ru<sup>3+</sup> salts were separately dispersed in ethylene glycol (EG) by sonication. EG was used as a solvent and served as an antioxidant to prevent the oxidation of colloidal **M** layers. During the mixing of two suspensions, oxygen-containing functional groups act as a surface-active agent to ruthenium chloride, which allows the adsorption of the positively charged metal ion (Ru<sup>3+</sup>) onto the negatively charged **M** surface via electrostatic interactions. Under the microwave irradiation, EG is decomposed to produce the *in-situ* reducing species CH<sub>3</sub>CHO (C<sub>2</sub>H<sub>6</sub>O<sub>2</sub> → CH<sub>3</sub>CHO + H<sub>2</sub>O) for the reduction of the Ru<sup>3+</sup> ions to *h*-phase ruthenium (*h*-Ru)



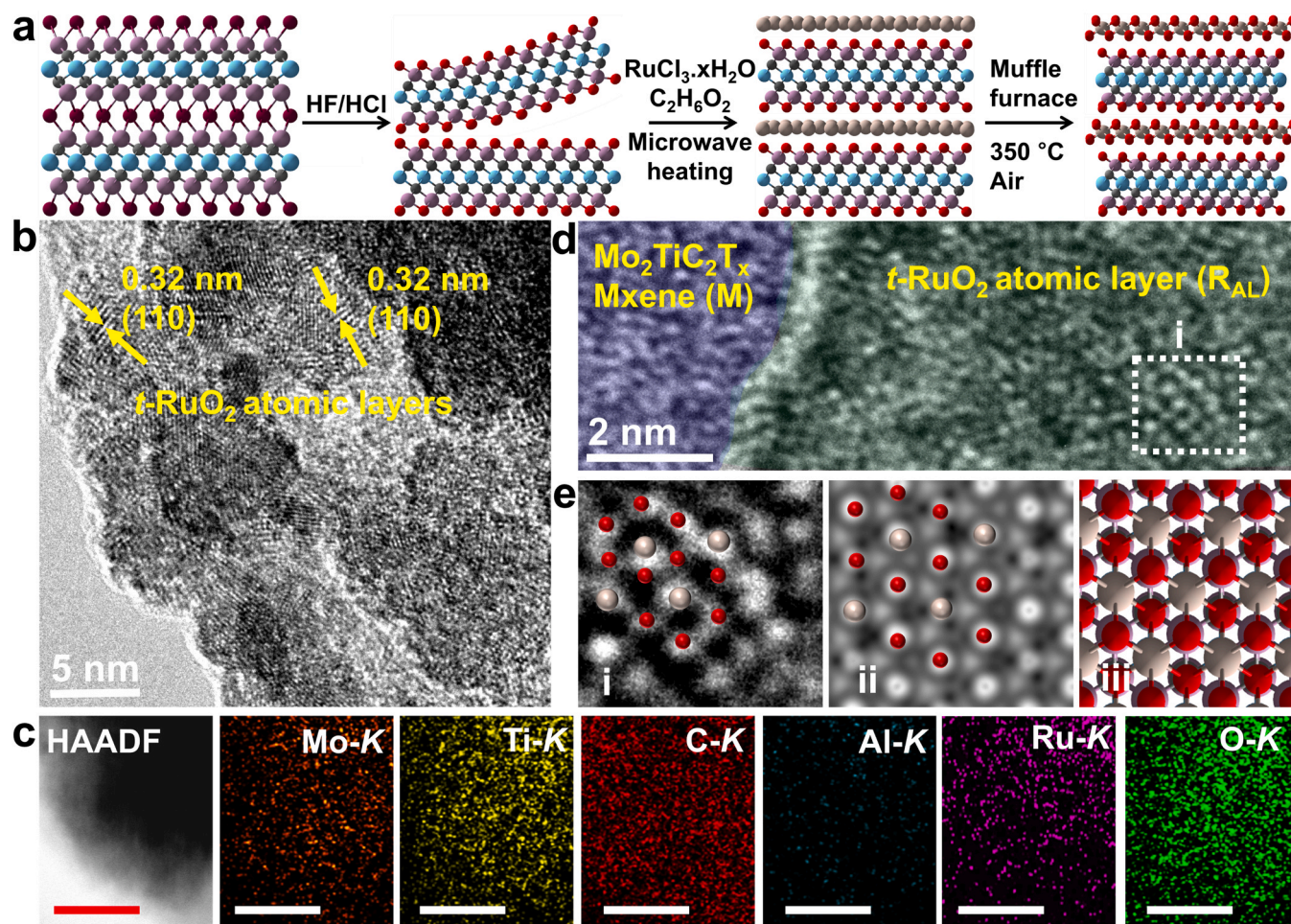


**Fig. 1.** Preparation and physical characterization of the  $R_{AL-M}$  electrocatalyst. **a**, Schematic representation of  $R_{AL-M}$  synthesis. **b**, High-resolution transmission electron microscopy (HRTEM) images of  $R_{AL-M}$ . **c**, High-angle annular dark-field scanning TEM (HAADF-STEM) image and corresponding element maps for Mo, Ti, C, Al, Ru, and O. Scale bars in 25 nm. **d**, HRTEM image of a distorted  $t$ -RuO<sub>2</sub> layer on the **M** substrate. **e**, Enlarged dotted region (i) in **d** and the corresponding simulated scanning TEM image (ii). The simulated image obtained by the theoretical model of  $R_{AL-M}$  (iii). The model and its simulated STEM image excellently matched the experimental HRTEM image. We used the above model for theoretical overpotential calculations. The beige/ivory, plum, deep sky, dark gray, red, dark purple, and cyan balls represent Ru, Mo, Ti, C, O, Al, and H atoms, respectively.

layers. The reduction process of  $Ru^{3+}$  ions by EG proceeds through two steps: (i) exchange of ligands around the  $Ru^{3+}$  ions and (ii)  $Ru^{3+}$  reduction to  $h$ -Ru layers on the **M** surface ( $6CH_3CHO + 2Ru^{3+} \rightarrow 2Ru + 6H^+ + 3CH_3COCOCH_3$ ). [50,51] Finally, the resulting powder was heated in air at a high temperature to achieve the desired product (denoted as  $R_{AL-M}$ ).

Note that  $h$ -Ru layers were transformed into  $t$ -phase RuO<sub>2</sub> layers during the oxidation process, which was confirmed by X-Ray diffraction (XRD) analysis. As shown in the XRD pattern of  $h$ -Ru/**M** (denoted as  $R_{AL-M_5}$ , Fig. S8c), the characteristic peaks at 38.4°, 42.2°, 44.1°, 58.3°, and 69.4°, which are corresponded to the (100), (002), (101), (102), and (110) plane of a typical hexagonal (Space group: P63/mmc; JCPDS No. 01-070-0274)  $h$ -Ru structure. The remaining peaks correspond to the **M** substrate (Fig. S8a, b, Note S2). After heating in air at 350 °C for 15 min (Fig. S8d), the diffraction peaks initiating at 28.0° (110), 35.1° (101), 40.0° (200), 45.0° (210), and 57.9° (220) confirm the existence of  $t$ -RuO<sub>2</sub> (space group P42/mnm; JCPDS No. 00-043-1027) and attest to the occurrence of the oxidizing process and transformation  $h$ -Ru phase to  $t$ -RuO<sub>2</sub> phase, which is also consistent with the molecular dynamics (MD) simulations results. MD calculations showed that  $h$ -phase RuO<sub>2</sub> is not stable under the O<sub>2</sub> environment and transforms into the  $t$ -phase of RuO<sub>2</sub> at 500 K (Figs. S9, S10, Video S1). To gain insight into the strong binding interactions between  $R_{AL}$  and **M** surfaces, we performed an interfacial charge-density difference and Bader charge analysis. The

charge-density difference study (Fig. S11a) shows significant charge transfer between  $R_{AL}$  and **M** surfaces. The Bader charge analysis further revealed that a net charge transfer of 0.37e<sup>-</sup> from **M** to  $R_{AL}$  surface is primarily liable for the strong interfacial interaction (Fig. S11b), which is consistent with our calculated  $R_{AL-M}$  heterostructure formation energy results (see Fig. S11a).

Supplementary material related to this article can be found online at [doi:10.1016/j.apcatb.2023.123139](https://doi.org/10.1016/j.apcatb.2023.123139).

To minimize the overpotential and maximize the mass activity for the OER, the heterostructure catalyst ( $R_{AL-M}$ ) was also synthesized using different temperatures and times (see Methods). The corresponding heterostructure catalysts are labeled as  $R_{AL}$  ( $t$ -RuO<sub>2</sub>-EG-350 °C-15 min),  $R_{AL-M_1}$  ( $t$ -RuO<sub>2</sub>-**M**-300 °C-15 min),  $R_{AL-M_2}$  ( $t$ -RuO<sub>2</sub>-**M**-400 °C-15 min),  $R_{AL-M_3}$  ( $t$ -RuO<sub>2</sub>-**M**-350 °C-10 min), and  $R_{AL-M_4}$  ( $t$ -RuO<sub>2</sub>-**M**-350 °C-20 min), and  $R_{AL-M_5}$  (**Ru-M**-EG). For comparison, the OER performances of commercial RuO<sub>2</sub> catalysts from two different companies and  $R_{AL-C}$  (RuO<sub>2</sub>-C) were investigated under similar conditions. X-ray photoelectron spectroscopy (XPS) was used to identify chemical species on the surfaces of all catalysts (Figs. S12-S19, Note S3). The commercial RuO<sub>2</sub> products are labeled as **C1-RuO<sub>2</sub>** (Pre-metek Co.) and **C2-RuO<sub>2</sub>** (Sigma-Aldrich). Since  $R_{AL-M}$  showed the best electrocatalytic activity, we focus our discussion on  $R_{AL-M}$ , unless specified otherwise (Figs. S20, S21). Scanning electron microscopy (SEM) and high-resolution transmission electron microscopy (HRTEM)



images show that  $R_{AL}$  is uniformly deposited on the surface of  $M$  (Fig. 1b, Fig. S22b,c). The SEM results reveal significant changes in the surface morphology because of the uniformly coated  $RuO_2$  on the  $M$  surface induced the thickness of  $M$  layers (Figs. S22a,b). The AFM image indicates the  $R_{AL}$  ( $RuO_2$  atomic layers) with a thickness of  $\sim 2.9$  nm, which is consistent with the previously reported data (Fig. S23). [52] The HRTEM image shows fringes with an interlayer spacing of  $\sim 0.32$  nm, which corresponds to the (110) plane of the distorted  $R_{AL}$  (Fig. 1b). The  $R_{AL}$  sheet size is varied from 5 to 20 nm (Fig. S22c). The high-angle annular dark-field scanning TEM (HAADF-STEM) image and the corresponding energy-dispersive X-ray spectroscopy (STEM-EDS) elemental mapping reveal that Mo, Ti, C, Ru, and O elements are evenly distributed over  $R_{AL}$ - $M$ , whereas trace amounts of Al are found because of the incomplete leaching of Al from  $M$  (Fig. 1c). The  $M$  (bright blue) and the distorted  $R_{AL}$  (bright green) areas are shown in the HRTEM image (Fig. 1d). The distorted  $R_{AL}$  area was further investigated to show the atomic planes more easily (Fig. 1e, i). These atomic planes (Fig. 1e, i) agree well with the simulated STEM image (obtained from the optimized structure using density functional theory (DFT)) (Fig. 1e, ii, iii), indicating the formation of  $R_{AL}$  on the surface of  $M$ . Inductively coupled plasma optical emission spectrometry (ICP-OES) results reveal that the mass loading of Ru is 1.76 wt% (Table S1).

X-ray absorption near-edge structure (XANES) spectroscopy was performed to examine the local structure around Ru atoms. The Ru K-edge XANES spectra of  $R_{AL}$ - $M$  and  $R_{AL}$  and  $C_2$ - $RuO_2$  showed peaks at 21036, 21160, and 21203 eV (Fig. 2a), which correspond to the spectral features of  $RuO_2$ . The changes in the intensity of the  $R_{AL}$ - $M$  post-edge peak are attributed to hybridization between the metal's 3d orbitals

and oxygen's 2p orbitals (see enlarged image of Fig. 2a). This also indicates that the 3d–4p transition and charge transfer from the O 2p→Ru 3d are enhanced with Mo/Ti ( $M$ ) due to the break of inversion symmetry of the oxygens around the Ru atoms. These evolutions reveal that the local geometry and structure of Ru have changed. The experimental Ru K-edge XANES spectra based on the Fourier transform (FT) of the extended XAFS (EXAFS) analysis further supported this result. The  $k^2$ -weighted Ru K-edge EXAFS spectrum of  $R_{AL}$ - $M$  and its fitted curve (Fig. 2b) exhibited a major peak at 2.03 Å, which is ascribed to the Ru–O bond in the first coordination shell with a coordination number (CN) of 1.7 (Table S3). The second dominant peak at 2.7 Å is interpreted as the second coordination shell (Ru–Ru bond) with a CN of 5.7. The Ru fit values illustrate that the CNs of Ru–O (1.8)/Ru–Ru (6.0) in  $R_{AL}$  (Fig. 2c, Table S3) is greater than those of  $R_{AL}$ - $M$  because of the polarization effects in the highly anisotropic surface of  $RuO_x$ . The best fit was obtained with a CN of 12 Ru atoms in the first shell at 2.7 Å (Ru–Ru), which is the ideal structure of 12 Ru atoms in the first coordination shell of Ru foil (Fig. S24, Table S3).

The normalized near-edge X-ray absorption fine structure (NEXAFS) is the most widely used to confirm the oxygen deficiencies on the surface of oxides.[52–55] NEXAFS spectra at O K-edge for  $R_{AL}$ - $M$ ,  $R_{AL}$ - $M_4$ ,  $R_{AL}$ - $M_5$ , and  $C_2$ - $RuO_2$  powders indicate the dipole electron transitions from O 1s core states to antibonding O 2p, which is hybridized with Ru 4d orbitals (Fig. 2d). The peaks located at 529.5 and 533.0 eV are ascribed to the electronic transition into  $t_{2g}$  ( $\pi$  overlap with oxygen 2p states) and  $e_g$  ( $\sigma$  overlap) states, respectively.[53–56] Close examination reveals (see a zoomed image of Fig. 2d) that the absorption white lines exhibit an increased total electron yield intensity in  $R_{AL}$ - $M_5$  compared to  $C_2$ - $RuO_2$ , which implies that the number of vacancies in the  $t_{2g}$  states is

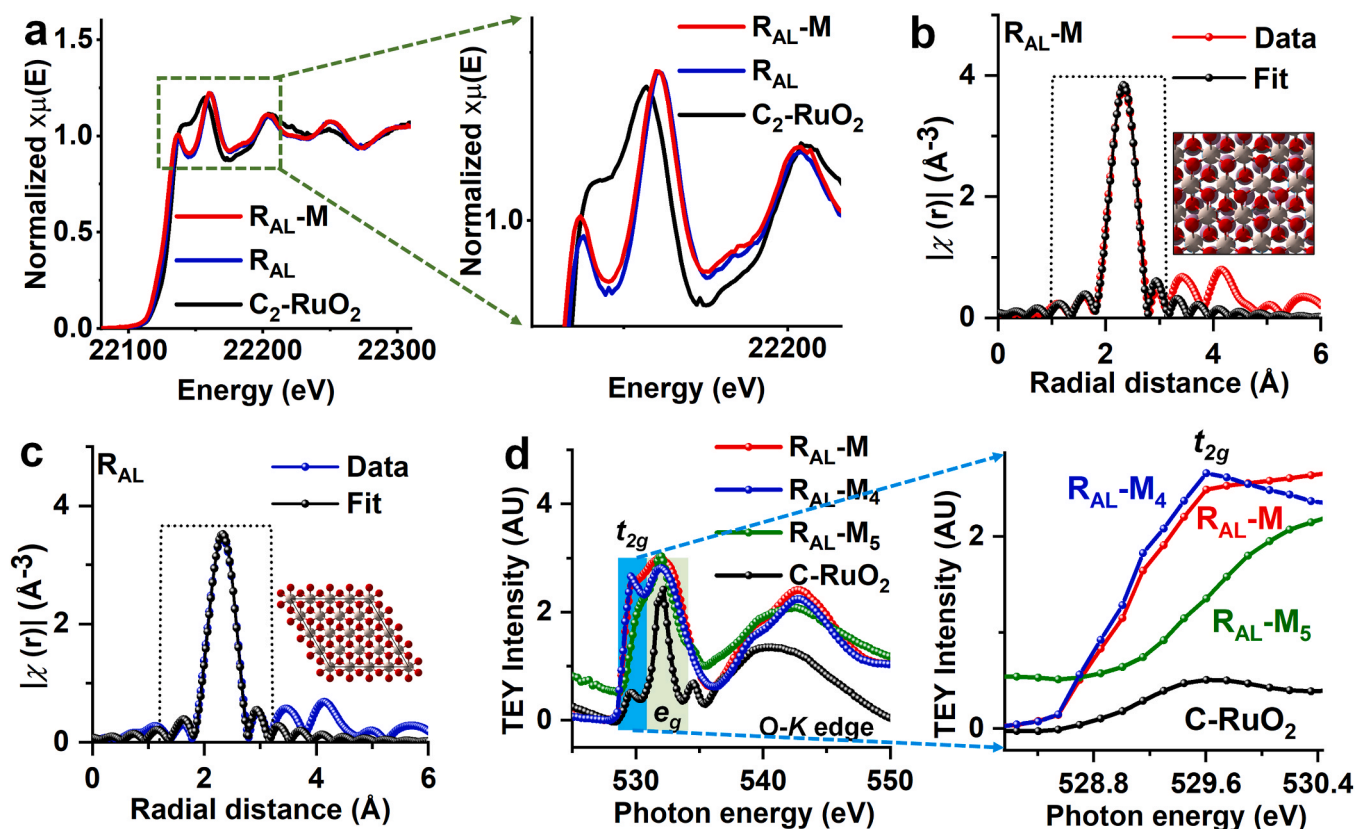


**Fig. 2.** Atomic-level structural of electrocatalysts. **a**, Ru K-edge X-ray absorption near-edge structure (XANES) spectra. Enlarged image of the dashed line area in Fig. 2a. **b**, **c**, Extended X-ray absorption fine structure (EXAFS) fitting curves of  $R_{AL}$ - $M$  and  $R_{AL}$  in R-space. The inset shows the proposed schematic model of  $R_{AL}$ - $M$  and  $R_{AL}$ . The beige/ivory, plum, deep sky, dark gray, red, and cyan balls represent Ru, Mo, Ti, C, O, and H atoms, respectively. **d**, Normalized near-edge X-ray absorption fine structure (NEXAFS) spectra at the O K-edge for  $R_{AL}$ - $M$ ,  $R_{AL}$ - $M_4$ ,  $R_{AL}$ - $M_5$ , and  $C_2$ - $RuO_2$  electrocatalysts. The shaded areas in light blue and bright green highlight  $t_{2g}$  and  $e_g$  regions, respectively. Enlarged image of the light blue area in Fig. 2d. AU: arbitrary units.

larger than that in the  $e_g$  states.[53–56] For  $R_{AL}-M$ , the number of vacancies in the  $t_{2g}$  states is larger than that in  $C_2-RuO_2$  but smaller than that in  $R_{AL}-M_4$ . The optimized vacancies in the  $t_{2g}$  state are favorable for the high catalytic activity toward the OER (Fig. S20b). Additionally, the energy difference between the unoccupied portion of the  $t_{2g}$  states to the  $e_g$  states of  $C_2-RuO_2$  is 3 eV (Fig. 2d), which coincides well with the band structure calculations. [57] In the case of  $R_{AL}-M$  and  $R_{AL}-M_4$ , the energy separation between the  $t_{2g}$  states and the  $e_g$  states is  $\sim 2.3$  eV, suggesting a strong hybridization with Mo 3d orbitals (Fig. 2d). Following that, the XPS core-level spectra of the O 1s lines in the different samples are employed to calculate the atomic concentration of oxygen vacancies on each surface.[58] We found that the amount of oxygen vacancies of catalysts is varied by changing the preparation conditions (Table S4). Consistent with the NEXAFS results, the optimized oxygen vacancy in  $R_{AL}-M$  shows a higher OER activity (Table S4, Fig. S20).

Further, projected density of states (PDOS; surface electronic structure) calculations also showed that the modulation of lattice oxygen vacancies in the  $R_{AL}-M$  had a significant effect on the electronic structure properties (Fig. S25a–c). Accordingly, only the double oxygen vacancies in  $R_{AL}-M$  possesses a DOS closer to the Fermi level ( $-0.07$  eV, optimized bonding states, Fig. S25b), while single oxygen vacancy possesses a DOS more downshift from the Fermi level ( $-0.15$  eV, strong bonding states; Fig. S25a). These results confirm that optimized oxygen vacancies show a highest electron-donating ability of the active center Ru atom, which can accelerate the electron transfer (charge-transfer) from the Ru site to adsorbates, resulting in a larger enhancement in OER catalytic activity. However, the three oxygen vacancies exhibited a strong antibonding state in  $R_{AL}-M$  (upshift from the Fermi level;  $0.12$  eV, Fig. S25c), suggesting a strong electron-accepting ability of the active center metal atom, and therefore, making it difficult to withdraw electrons from the active center intermediates, representing a lower OER activity.

The chemical compositions of  $M$ ,  $R_{AL}-M_5$ , and  $R_{AL}-M$  were analyzed by high-resolution XPS (Fig. 3). The binding energy and intensity (Figs. 3a and 3d) revealed the Mo and Ti peaks for  $M$  to be mainly

$Mo^{4+}/Ti^{2+}$  with a small amount of  $Mo^{5+}/Mo^{6+}/Ti^{3+}/Ti^{4+}$ , indicating the surface oxidation during the preparation of one or a few layers of  $M$ . [59–61] The Mo 3d<sub>5/2</sub> components are located at binding energies 229.5, 230.2, and 232.6 eV, which are associated with oxidation states of  $Mo^{4+}$ ,  $Mo^{5+}$ , and  $Mo^{6+}$ , respectively. [59,60] The  $Ti^{2+}$ ,  $Ti^{3+}$  and  $Ti^{4+}$  peaks are centered at 455.7, 457.3, and 458.6 eV, respectively (Fig. 3d). [61] After Ru layers deposition under the action of microwave heat radiation, the binding energies of Mo/Ru shifted toward higher positions at 229.6/232.7 eV ( $Mo^{4+}$ ), 232.6/235.7 eV ( $Mo^{6+}$ ), and 462.6/284.8 eV ( $Ru^{4+}$ ), which suggests the formation of  $MoO_2/-MoO_3/RuO_2$  due to the presence of atmospheric air (Fig. 3b and 3e). [59, 62,63] A strong peak is located at  $\sim 461.5/483.7$  eV from the metallic Ru ( $Ru^0$ ). The weak peaks of metallic Mo (227.9/231.0 eV) [64] and oxidized  $Ti^{4+}$  ( $TiO_2$ ) are also show in Figs. 3b and 3e. After heating in air at 350 °C, the binding energy and intensity (Figs. 3c and 3f) show the Mo and Ti peaks for  $R_{AL}-M$  to be largely  $Mo^{5+}/Mo^{6+}/Ti^{4+}$  with a tiny amount of  $Mo^{4+}$ , suggesting the Ti and Mo are completely oxidized during the oxidation process of the  $R_{AL}-M_5$  catalyst.[59–65] The high-resolution Ru 3p spectrum shows a pair of spin-orbit split components at 462.4 and 484.6 eV, assigned to the Ru 3p<sub>3/2</sub> and Ru 3p<sub>1/2</sub> of oxidized Ru ( $RuO_2$ ), respectively, while the peaks centered at 465.5 and 487.7 eV are assigned to satellite peaks. After oxidation, a pair of new peaks are also observed at 463.4 and 485.6 eV in Fig. 3f, corresponding to the formation of  $Ru\delta^+$  ( $4 < \delta$ ). [66] The electronic structure change, following the deposition and oxidation processes, is reflected in the change of the Mo 3d, Ti 2p, and Ru 3p regions. This suggests that  $R_{AL}-M_5$  is completely oxidized by atmospheric oxygen. Additionally, the high-resolution Mo 3d and Ru 3p spectra of  $R_{AL}-M$  are related to the individual contributions of the data from  $MoO_2/MoO_3$  ( $Mo^{4+}$ ,  $Mo^{5+}$ , or  $Mo^{6+}$ ; Fig. 3c) [55,56] and  $RuO_2/Ru\delta^+$  ( $Ru^{4+}$  or  $Ru^{>4+}$ ; Fig. 3f), confirming the presence of high-valence species in  $R_{AL}-M$  (Fig. 3c and 3f). [59,60,62–66].

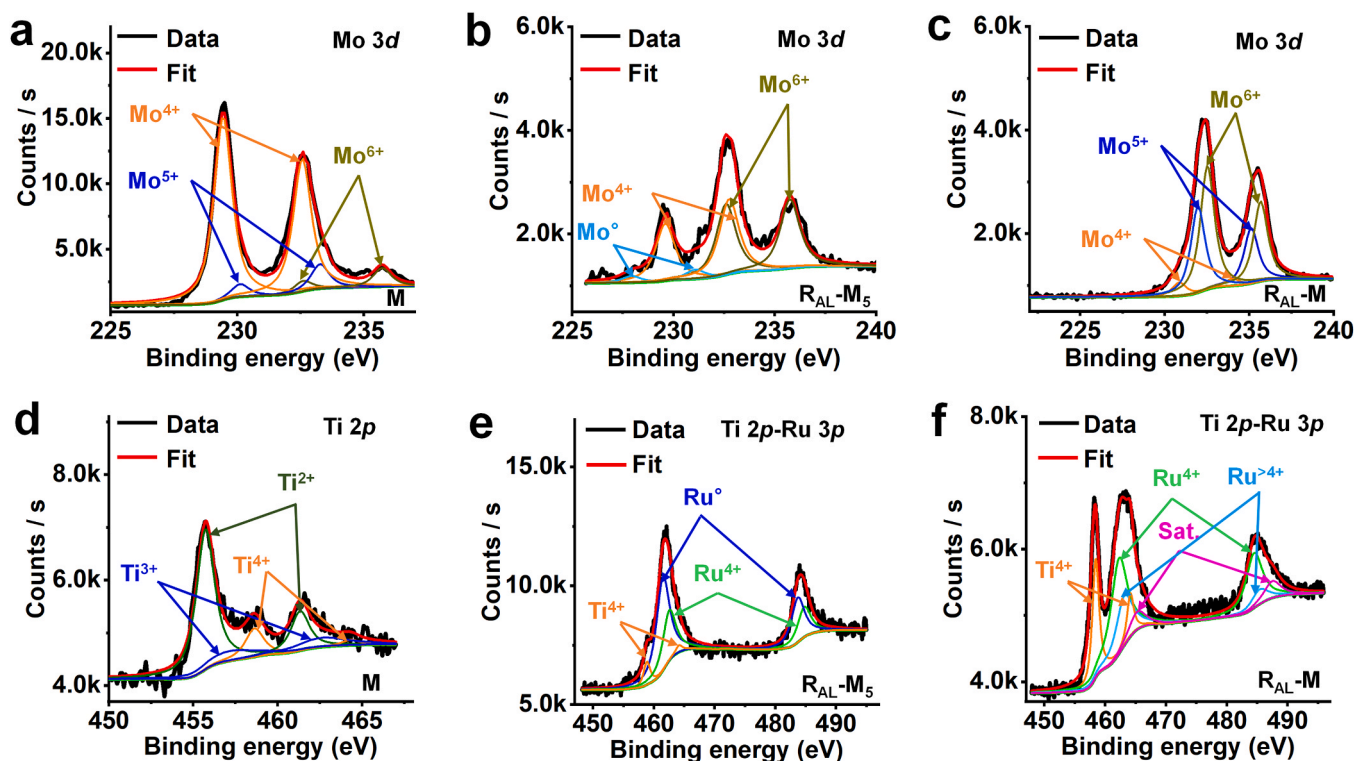


Fig. 3. Chemical characterization. a–c, Mo 3d high-resolution X-ray photoelectron spectroscopy (HRXPS) spectra of  $M$ ,  $R_{AL}-M_5$ , and  $R_{AL}-M$ . d, Ti 2p HRXPS spectra of  $M$ . e, f, Ti 2p–Ru 3p HRXPS spectra of  $R_{AL}-M_5$  and  $R_{AL}-M$ .

### 3.2. Analysis of electrocatalytic performance

The OER tests of  $R_{AL-M}$  and five reference catalysts—two commercial- $RuO_2$  ( $C_1-RuO_2$ ,  $C_2-RuO_2$ ),  $R_{AL-C}$ ,  $R_{AL}$ ,  $M$ , and graphite sheet—were measured for comparison. The OER performances were assessed using a standard three-electrode cell in an  $O_2$ -saturated 0.5 M  $H_2SO_4$  (0.48 pH; Fig. S26) to ensure the  $O_2/H_2O$  equilibrium for the OER. [67].

The linear sweep voltammetry (LSV) plots indicated that  $R_{AL-M}$  has the most active polarization curve with a low overpotential of  $222 \pm 1$  mV to achieve the current density of  $10 \text{ mA cm}^{-2}$  (Fig. 4a, Fig. S21). The minuscule Tafel slope of  $50.4 \text{ mV dec}^{-1}$  was obtained for  $R_{AL-M}$ , compared to those calculated for  $C_1-RuO_2$  ( $66.6 \text{ mV dec}^{-1}$ ),  $C_2-RuO_2$  ( $88 \text{ mV dec}^{-1}$ ), and  $R_{AL}$  ( $54.1 \text{ mV dec}^{-1}$ ) (Fig. 4b), indicating that the surface environment of  $R_{AL-M}$  is kinetically more favorable for OER activity. According to the Arrhenius plot results (Figs. S27, S28d), the activation energy of the  $R_{AL-M}$  electrocatalyst downshifted to  $15.48 \text{ kJ mol}^{-1}$  relative to that of  $R_{AL}$  ( $17.87 \text{ kJ mol}^{-1}$ ) and  $C_1-RuO_2$  ( $20.85 \text{ kJ mol}^{-1}$ ) at 1.45 V (versus reversible hydrogen electrode; RHE), further verifying the faster OER kinetics after the incorporation of high-valence Mo/Ti active sites onto the  $M$  surface. More importantly,  $R_{AL-M}$  shows the highest mass activity of  $6.2 \text{ A mg}_{Ru-metal}^{-1}$  at 1.50 V versus RHE, which is 150 and 540 times higher than those of industrial

( $0.041 \text{ A mg}_{Ru-metal}^{-1}$ ,  $C_1-RuO_2$  and  $0.012 \text{ A mg}_{Ru-metal}^{-1}$ ,  $C_2-RuO_2$ ) catalysts, respectively, and surpasses previously reported activities (Fig. 4c, Table S2). Notably, the turnover frequency (TOF) of  $R_{AL-M}$  is  $2.35 \text{ O}_2 \text{ s}^{-1}$ , which is 150 and 540 times higher than those of ( $0.015 \text{ O}_2 \text{ s}^{-1}$ )  $C_1-RuO_2$  and ( $0.0043 \text{ O}_2 \text{ s}^{-1}$ )  $C_2-RuO_2$ , respectively, at 1.50 V versus RHE in the acidic electrolyte (Fig. 4d, Table S5), suggesting a greater intrinsic capacity for electrocatalytic oxygen production. In addition, we further evaluated the electrochemically active surface area (ECSA) (Figs. S29, S30) and roughness factors of  $R_{AL-M}$ ,  $R_{AL}$ ,  $C_1-RuO_2$ , and  $C_2-RuO_2$  catalysts and plotted the LSVs with respect to the ECSA (Figs. S31a and Table S5). The results showed not only that the OER performance of the  $R_{AL-M}$  is enhanced by the ECSA but also that the intrinsic activity arising from the high-valent Mo-species substrate (Table S5). To clarify the effect of working electrodes (GCE;  $0.196 \text{ cm}^2$  and graphite sheet;  $1 \times 2 \text{ cm}^2$ ), the overpotentials of  $R_{AL-M}$ ,  $R_{AL}$ ,  $C_1-RuO_2$ , and  $C_2-RuO_2$  catalysts were assessed at a current density of  $10 \text{ mA cm}^{-2}$  in the LSV curves. Both working electrodes showed a similar overpotential,  $222 \pm 1$  mV, at  $10 \text{ mA cm}^{-2}$  (Fig. 4a, Fig. S31b), indicating that the switching of working electrodes has no effect. To ensure the effects of  $HSO_4^-$ ,  $SO_4^{2-}$ , and  $ClO_4^-$  anions, the electrocatalytic performance of  $R_{AL-M}$  was recorded in comparison with that of the commercial  $C_2-RuO_2$  catalyst in 0.5 M  $HClO_4$  and 0.5 M  $H_2SO_4$  (Fig. S32). The small changes in the overpotential indicate that the anions ( $HSO_4^-$ ,  $SO_4^{2-}$ , and  $ClO_4^-$ ) do not

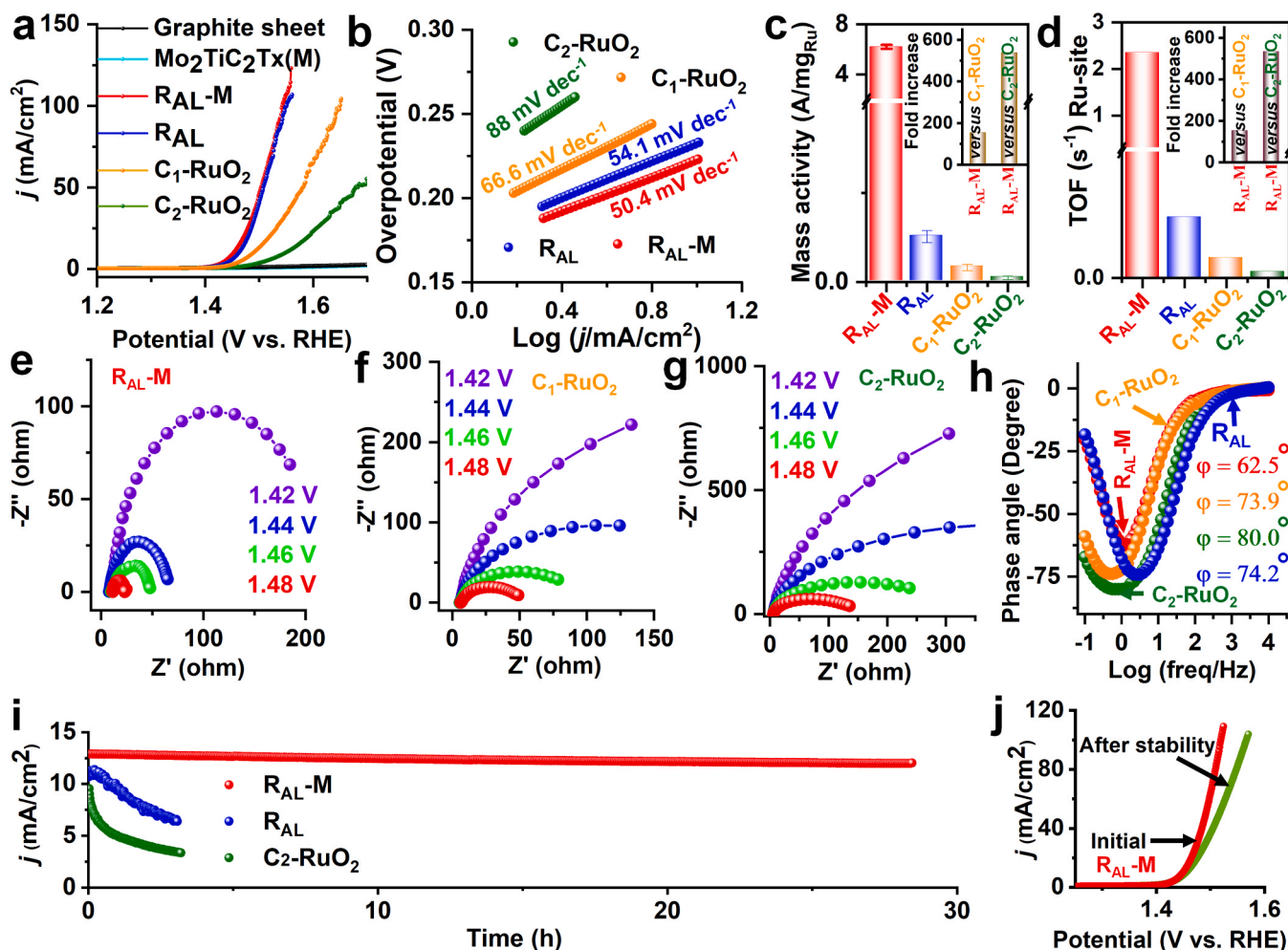


**Fig. 4.** Electrocatalytic OER performances and *in-situ* electrochemical impedance spectroscopy (EIS) measurements in 0.5 M  $H_2SO_4$  at 25 °C. **a**, OER linear sweep voltammetry (LSV) curves (scan rate  $2 \text{ mV s}^{-1}$ ). **b**, Tafel plots. **c**, **d**, Mass activity and turnover frequency (TOF) at an applied potential of 1.5 V versus RHE. The mass activities and TOF were calculated based on the Ru metal. The error bars represent the standard deviation of the measurements. **e**–**g**, Nyquist plots for  $R_{AL-M}$ ,  $C_1-RuO_2$ , and  $C_2-RuO_2$  electrocatalysts (GCE area:  $0.196 \text{ cm}^2$ ) at different applied potentials. **h**, Bode plot of phase angle versus frequency for  $R_{AL-M}$ ,  $R_{AL}$ ,  $C_1-RuO_2$ , and  $C_2-RuO_2$  electrocatalysts in the frequency range of  $10^5$ – $0.1 \text{ Hz}$  (GCE area:  $0.196 \text{ cm}^2$ ). **i**, Chronoamperograms of  $R_{AL-M}$ ,  $R_{AL}$ , and  $C_2-RuO_2$  catalysts at applied potentials of 1.453, 1.463, and 1.550 V, respectively. **j**, OER LSV curves before and after stability testing.



affect the catalytic behavior of  $\mathbf{R_{AL-M}}$  (Fig. S32a), while the commercial  $\mathbf{C_2-RuO_2}$  catalyst showed a drastic change in the overpotential due to the stronger adsorption of  $\text{HSO}_4^-$  and  $\text{SO}_4^{2-}$  anions on the  $\text{RuO}_2$  (110) surface compared to the adsorption of  $\text{ClO}_4^-$  anions (Fig. S32b). All the Nyquist plots display a depressed semicircle, suggesting a charge-transfer process during the OER (Fig. S33). These Nyquist plots were further fitted to analyze the charge-transfer resistance by a simple equivalent electrical circuit (Inset of Fig. S33). Notably,  $\mathbf{R_{AL-M}}$  exhibits the smallest semicircle diameter compared with other catalysts, implying the smallest electric resistance and the fastest charge-transfer rate at the interface (Fig. S33, Table S5). To understand the adsorption and desorption kinetics of the oxygen-containing reactive species on the surfaces of  $\mathbf{R_{AL-M}}$ ,  $\mathbf{C_1-RuO_2}$ ,  $\mathbf{C_2-RuO_2}$ , and  $\mathbf{R_{AL}}$ , *in-situ* electrochemical impedance spectroscopy (EIS) tests were conducted at different applied potentials (Fig. 4e–g, Fig. S34). The measured impedance of the acidic OER process on the  $\mathbf{R_{AL-M}}$ ,  $\mathbf{R_{AL}}$ ,  $\mathbf{C_1-RuO_2}$ , and  $\mathbf{C_2-RuO_2}$  catalysts was recorded from 1.42 to 1.48 V (versus RHE). Through the direct altering trend and the diameter of the semicircle in the Nyquist plots, faster kinetics and adsorption of reactants with rising potentials were revealed.  $\mathbf{R_{AL-M}}$  displays faster reaction kinetics, which is ascribed to the larger number of Ru active sites and the strong  $\mathbf{M}$  coupling effect. The relaxation time constant of the  $\mathbf{R_{AL-M}}$  catalyst ( $\tau_0 = 1/f_0$ , where  $f_0$  is the frequency at a phase angle of  $-45^\circ$ ) equals 2.6 s. The fast frequency response of  $\mathbf{R_{AL-M}}$  is attributed to the large and accessible surface area. The phase angle of  $\mathbf{R_{AL-M}}$  ( $62.5^\circ$ ) is much smaller than those of  $\mathbf{R_{AL}}$  ( $74.2^\circ$ ),  $\mathbf{C_1-RuO_2}$  ( $73.9^\circ$ ), and  $\mathbf{C_2-RuO_2}$  ( $80.0^\circ$ ) catalysts (Fig. 4h), indicating low charge-transfer resistance, which facilitates the adsorption and desorption of reactants due to the very short diffusion distance.

### 3.3. Evaluation of catalyst durability

Durability is one of the key points when considering large-scale industrial implementation since most metal oxides show a significant activity loss under acidic OER conditions (working electrode area;  $1 \text{ cm}^2$ ). In a proof-of-principle demonstration of its industrial use, we studied the catalytic performance of  $\mathbf{R_{AL-M}}$  in three- and two-electrode configurations (Fig. 4i, Fig. S28a,b). In the three-electrode cell,  $\mathbf{R_{AL-M}}$  retained 92% of the OER activity under the applied potential of 1.45 V after the 28 h durability test, whereas  $\mathbf{R_{AL}}$  and  $\mathbf{C_2-RuO_2}$  catalysts degraded dramatically (Fig. 4i). The LSV curves before and after the durability test exhibited an insignificant change ( $\sim 0.05 \text{ V}$  at  $100 \text{ mA cm}^{-2}$ ) for the  $\mathbf{R_{AL-M}}$  catalyst (Fig. 4j).

To gain a deeper understanding of the  $\mathbf{R_{AL-M}}$  catalyst degradation mechanism, the XPS analyses were conducted before and after 14-h/18-h durability test (Fig. 3c,f, and Figs. S12, S35, S36, Note 3). The XPS surface analyses reveal that the mixed oxidation states of the cationic valences (Mo: 4+, 5+ 6+, Ti: 4+, and Ru 4+ and >4+) presented in the  $\mathbf{R_{AL-M}}$  before and after the OER reaction (Fig. 3c,f, and Figs. S12, S35, S36, Note 3). During surface cation exchange, the high oxidation states of Mo/Ti/Ru cations are more susceptible to electrons from adsorbed oxygen species. Once the electron from the adsorbed oxygen species is transferred to the metal cation, the cation will be reduced and will return to the initial oxidation state. [68] In this way, a surface cation exchange is established for each elementary step, resulting in remarkable electrocatalytic mass activity and stability obtained for the optimized  $\mathbf{R_{AL-M}}$  catalyst.

Besides, it is known that Ru centers are oxidized to  $\text{Ru} > 4+$  at potential excursions higher than 1.4 V. [69] The highly oxidized  $\mathbf{R_{AL}}$  and  $\mathbf{C_2-RuO_2}$  are unstable due to absence of  $\mathbf{M}$  substrate (Fig. 4i). The incorporation of Mo/Ti ( $\mathbf{R_{AL-M}}$ ) allows the stabilization of  $\text{Ru} > 4+$  ions within the lattice. As a result, versatile Ru catalytic centers is facily increase or decrease their charge depending on the adsorbates, which is beneficial for the OER.

After 14 h and 18 h durability test, another important observation is the O 1 s peaks shifted to higher binding energy compared to the initial

sample (Figs. S12c, S35e, S36e, Table S4, and Note S3), which is beneficial for modulating the electronic structure and accelerating electron transfer, thus resulting in improved activity and stability for OER. Additionally, oxygen vacancies also appear on the  $\mathbf{R_{AL-M}}$  surface before (17.7 at%) and after the OER process due to the conservation of charge between Mo/Ti and Ru ions. After the 14 h OER test, the peak associated with the oxygen vacancies increased sharply (22.5 at%), while after the 28-h OER test it decreased sharply (6.6 at%) (see Table S4). These changes occur due to the self-healing of the oxygen vacancies, where oxygen vacancies are restored by the capturing of oxygen atoms from the adsorbed water molecules. [70] This surface reconstruction process produces highly catalytic active sites for OER.

Further, the chronopotentiometry test (two-electrode cell) in the presence (10 K second) and absence (22 h) of the membrane at a current density of  $10 \text{ mA cm}^{-2}$  indicated the exceptional stability of  $\mathbf{R_{AL-M}}$  (Fig. S28a,b). Both cases showed small changes in potential (94% retained after 10 K and 22 h), which are requirements for practical implementation. Furthermore, the ionic conductivity of the electrolyte is similar during the stability test (Fig. S28a). The day-dependent LSV test revealed no significant changes in OER activity after 21 days (Fig. S28c). SEM, TEM, and HRTEM images show that the surface structure is mostly maintained after the long-term stability test under the current density of  $10 \text{ mA cm}^{-2}$  (Figs. S37, S38a,b,d). TEM-EDX mapping confirms the uniform distribution of Mo, Ti, C, Ru, and O in  $\mathbf{R_{AL-M}}$  after the stability test (Fig. S38c). Moreover, the diffraction peak positions of  $\mathbf{R_{AL-M}}$  catalyst are the same before and after the OER stability test (Fig. S39), indicating the unchanged surface structure. It is strongly suggesting that the  $\mathbf{M}$  support structure is stable during the long OER stability test. ICP-OES was performed to examine the amounts of Ru, Mo, and Ti ions dissolved in  $\mathbf{R_{AL-M}}$  after the long-term stability test at a current density of  $10 \text{ mA cm}^{-2}$ . Traces of dissolved Ru, Mo, and Ti ions were detected for  $\mathbf{R_{AL-M}}$  after the 22-h stability test (Table S6), indicating its remarkable resistance to acid corrosion due to the surface cation exchange between the oxidation states of the cationic valences (Mo: 4+, 5+, 6+; Ti: 4+, Ru: 4+, >4+) during the operation (Fig. S40, Note S3), which is consistent with the durability test for a three-electrode cell system [22,59–65,69].

### 3.4. Theoretical studies on OER activity

To further understand the synergy between  $\mathbf{R_{AL}}$  and  $\mathbf{M}$  structures, we conducted DFT calculations [71,72] and proposed different models (see computational methods and Fig. S5). The DFT results revealed that the  $\mathbf{R_{AL-M}}$  model excellently matched with the results of HRTEM and EXAFS (Figs. 1e and 2b). By analyzing the geometric parameter, we found that the OER at interface region of the  $\mathbf{R_{AL-M}}$  catalyst is not feasible due to small interlayer distance of  $3.18 \text{ \AA}$ . The Fig. S41 demonstrates the key intermediates ( $\text{O}^*/\text{HO}^*$  and  $\text{HOO}^*$ ) involved in OER are larger in size and cannot bind at the interface region. Therefore, we did not consider the interfacial active sites between  $\mathbf{R_{AL}}$  and  $\mathbf{M}$  layers.

To examine the OER activity, we systematically studied the AEM and LOM at zero and applied potentials. The adsorption free energies of OER intermediates ( $\text{O}^*$ ,  $\text{OH}^*$ ,  $\text{OOH}^*$ , and  $\text{H}^*$ ) adsorbed at Ru/Mo or O active sites were calculated considering a pure implicit solvation model with a water dielectric constant ( $\epsilon_{\text{H}_2\text{O}} = 80$ ). In addition, we explicitly modeled the  $\mathbf{R_{AL-M}}$  surface with five layers of water and showed that the adsorption free energies are comparable with the implicit solvation model (Tables S7, S8 and Fig. S42). The AEM solely focuses on the redox activity of Ru/Mo or O active sites at the catalyst surface and involves four consecutive proton-coupled electron transfer steps, whereas the LOM involves the generation of oxygen vacancy sites at the surface (Fig. 5a). The DFT results revealed that both the AEM and the LOM with the Ru active site show  $\text{HOO}^*$  formation (Step 3) as the potential determining step (PDS), while the O active site shows  $\text{HO}^*$  adsorption (Step 1) as the PDS. Remarkably, the  $\mathbf{R_{AL}}$  catalyst shows that the  $\text{HO}^*$  adsorption (Step 1) has the highest energy barrier for both Ru and

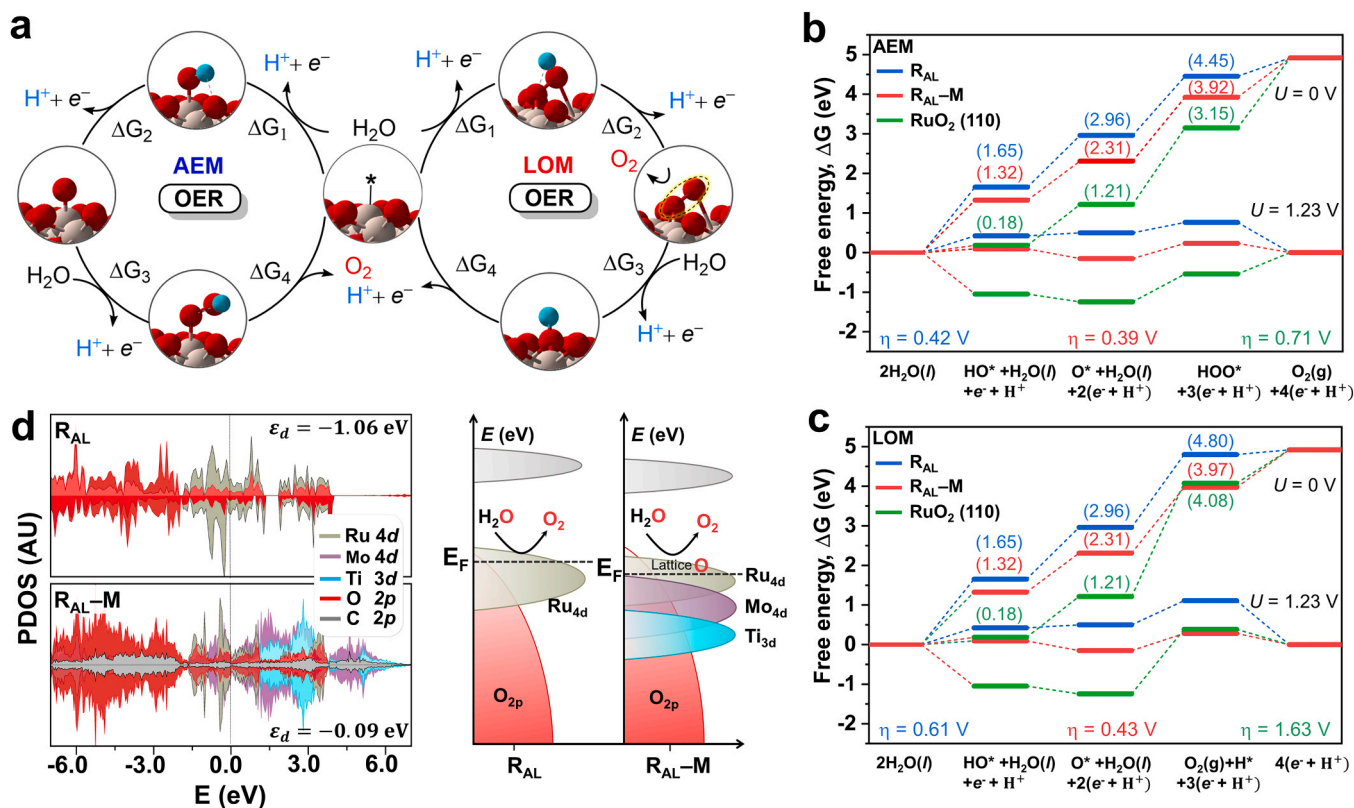


**Fig. 5.** Oxygen evolution reaction (OER) mechanism and theoretical investigations. **a**, Schematic illustration of the adsorbate evolving mechanism (AEM) and lattice oxygen oxidation mechanism (LOM) of the OER. The four electrochemical reaction steps for each mechanism are shown, where “\*” denotes the catalyst surface before the adsorption of OER intermediates. **b**, Free energy diagram of OER via the AEM and LOM pathways at the Ru active site for  $\text{R}_{\text{AL}}$ ,  $\text{R}_{\text{AL-M}}$ , and five-layered rutile  $\text{RuO}_2(110)$  surface. **c**, Projected density of states (PDOS) and schematic diagrams of rigid band models for  $\text{R}_{\text{AL}}$  and  $\text{R}_{\text{AL-M}}$  toward acidic OER (AU: arbitrary units). The dashed line denotes the Fermi energy ( $E_F$ ). The localized Ru (4d) states [ $\text{R}_{\text{AL}}$  ( $\epsilon_d = -1.06$  eV) to  $\text{R}_{\text{AL-M}}$  ( $\epsilon_d = -0.09$  eV)] and partially occupied O (2p) band states near Fermi level in  $\text{R}_{\text{AL-M}}$  catalyst manifest that both the AEM and LOM pathways are responsible for the enhanced OER activity. The beige/ivory, plum, deep sky, dark gray, red, and cyan balls represent Ru, Mo, Ti, C, O, and H atoms, respectively.

O active sites. We further compared the reaction free energies (Table S9) of AEM and LOM pathways, Fig. 5b demonstrates that the AEM is much preferred over the LOM with relatively lower thermodynamic barriers at Ru and O active sites. For  $\text{R}_{\text{AL-M}}$ , the theoretical overpotential ( $\eta$ ) related to the PDS is calculated to be 0.39 V (AEM)/0.43 V (LOM) (implicit solvation model), which is much lower than that of  $\text{Mo}_2\text{TiC}_2\text{O}_2$  (1.34 V/1.34 V), commercial  $\text{RuO}_2$  (0.71 V/1.63 V), and  $\text{R}_{\text{AL}}$  (0.42 V/0.61 V). The  $\text{R}_{\text{AL-M}}$  exhibits a lower overpotential of 0.39 V via the AEM pathway with a small activation barrier (0.29 eV) in the PDS, which is surmountable at room temperature (Fig. S43). The outstanding theoretical  $\eta$  of  $\text{R}_{\text{AL-M}}$  explains the minuscule onset overpotential of 0.18 V versus RHE required in the OER measurement. The theoretical  $\eta$  of  $\text{R}_{\text{AL-M}}$  is estimated to be 0.44 V in the presence of water (explicit solvation model) [73], which is comparable to the results obtained using the implicit solvation model. The small overpotentials (AEM/LOM reaction pathways) of  $\text{R}_{\text{AL-M}}$  indicate that the OER mechanism involves the AEM and LOM pathways after the introduction of **M**. In contrast,  $\text{R}_{\text{AL}}$  and  $\text{RuO}_2$  proceed through the AEM. The projected density of states (PDOS) further implies that the Ru/Mo (4d) band states near the Fermi level endow the AEM as the favored pathway in  $\text{R}_{\text{AL}}$ , **M**,  $\text{R}_{\text{AL-M}}$ , and  $\text{RuO}_2$  with Ru/Mo as the main active site of the OER (Fig. 5c). Moreover, the total *d*-band center value of ( $\epsilon_d = -0.09$  eV) and partially occupied O (2p) band states near the Fermi level in the  $\text{R}_{\text{AL-M}}$  model manifest that the direct O–O coupling is significantly facilitated, which no longer limits the reaction for the LOM pathway (Fig. 5c, Fig. S44). Thus, both the AEM and LOM pathways are responsible for the superior OER activity of the  $\text{R}_{\text{AL-M}}$  catalyst.

#### 4. Conclusion

We prepared evenly distributed  $\text{R}_{\text{AL}}$  on the surface of **M** as an anodic electrode material for acidic water splitting applications. The unique properties of  $\text{R}_{\text{AL}}$  eliminated the mass activity and lifetime issues of acidic water electrolysis. The high surface state of Ru is protected by high-valence Mo ions ( $\text{Mo}^{4+}$ ,  $\text{Mo}^{5+}$  or  $\text{Mo}^{6+}$ ) formed during the OER process via surface cation exchange in the acidic solution, resulting in the prolonged catalyst lifetime. DFT results revealed that the most favorable mechanism for the OER over the Ru active sites is the AEM. The incorporation of **M** promotes the formation of high-valence Mo/Ti species and the LOM of  $\text{R}_{\text{AL-M}}$ , further accelerating the reactions. This work not only offers an ideal process for oxygen generation in strongly acidic media but also provides insights into realizing large-scale low-cost catalyst production using various materials.

#### CRediT authorship contribution statement

**Jitendra N. Tiwari:** Conceptualization, Methodology, Formal analysis, Investigation, Data curation, Writing – original draft, Writing – review & editing, Supervision, Funding acquisition. **Muhammad Umer:** Data curation, Computation. **Gokul Bhaskaran:** Data curation, Visualization. **Sohaib Umer:** Computation, Visualization. **Geunsik Lee:** Validation, Visualization. **Min Gyu Kim:** Data curation. **Han-Koo Lee:** Data curation. **Krishan Kumar:** Visualization. **A.T. Ezhil Vilian:** Visualization. **Yun Suk Huh:** Writing – original draft, Writing – review & editing, Supervision, Funding acquisition. **Young-Kyu Han:** Writing – original draft, Writing – review & editing, Supervision, Funding acquisition.

## Declaration of Competing Interest

The authors declare that they have no known competing financial interests or personal relationships that could have appeared to influence the work reported in this paper.

## Data Availability

Data will be made available on request.

## Acknowledgements

This work was supported by Basic Science Research Program through the National Research Foundation of Korea (NRF) funded by the Ministry of Education (NRF-2022R1A2C1006645, NRF-2022M3J7A1062940, NRF-2022R1A2C2008968, and NRF-2021M3H4A1A02055684) and the supercomputing resources including technical support are from the National Supercomputing Center KISTI (KSC-2023-CRE-0063, KSC-2021-CRE-0567, KSC-2023-CRE-0067).

## Appendix A. Supporting information

Supplementary data associated with this article can be found in the online version at doi:10.1016/j.apcatb.2023.123139.

## References

- M.R. Kandel, U.N. Pan, P.P. Dhakal, R.B. Ghising, T.T. Nguyen, J. Zhao, N.H. Kim, J.H. Lee, Unique heterointerface engineering of Ni<sub>2</sub>P–MnP nanosheets coupled Co<sub>2</sub>P nanoflowers as hierarchical dual-functional electrocatalyst for highly proficient overall water-splitting, *Appl. Catal. B Environ.* 331 (2023), 122680.
- J. Goldemberg, Ethanol for a sustainable energy future, *Science* 315 (2007) 808–810.
- C.-L. Huang, Y.-G. Lin, C.-L. Chiang, C.-K. Peng, D.S. Raja, C.-T. Hsieh, Y.-A. Chen, S.-Q. Chang, Y.-X. Yeh, S.-Y. Lu, Atomic scale synergistic interactions lead to breakthrough catalysts for electrocatalytic water splitting, *Appl. Catal. B Environ.* 320 (2023), 122016.
- H. Dotan, et al., Decoupled hydrogen and oxygen evolution by a two-step electrochemical-chemical cycle for efficient overall water splitting, *Nat. Energy* 4 (2019) 786–795.
- B. Zhang, et al., Homogeneously dispersed multimetal oxygen-evolving catalysts, *Science* 352 (2016) 333–337.
- T.M. Gür, Review of electrical energy storage technologies, materials and systems: challenges and prospects for large-scale grid storage, *Energy Environ. Sci.* 11 (2018) 2696–2767.
- J.N. Tiwari, S. Sultan, C.W. Myung, et al., Multicomponent electrocatalyst with ultralow Pt loading and high hydrogen evolution activity, *Nat. Energy* 3 (2018) 773–782.
- X.M. Xu, Y. Pan, L. Ge, et al., High-performance perovskite composite electrocatalysts enabled by controllable interface engineering, *Small* 17 (2021) 2101573.
- X.M. Xu, Z.P. Shao, S.P. Jiang, High-entropy materials for water electrolysis, *Energy Technol.* 10 (2022) 2200573.
- X.M. Xu, H.N. Sun, S.P. Jiang, Z.P. Shao, Modulating metal–organic frameworks for catalyzing acidic oxygen evolution for proton exchange membrane water electrolysis, *SusMat* 1 (2021) 460–481.
- J. Tang, X.M. Xu, T. Tang, Y. Zhong, Z.P. Shao, Perovskite-based electrocatalysts for cost-effective ultrahigh-current-density water splitting in anion exchange membrane electrolyzer cell, *Small Methods* 6 (2022) 2201099.
- H.N. Nong, et al., Key role of chemistry versus bias in electrocatalytic oxygen evolution, *Nature* 587 (2020) 408–413.
- J. Feng, et al., Iridium-based multimetallic porous hollow nanocrystals for efficient overall-water-splitting catalysis, *Adv. Mater.* 29 (2017) 1703798.
- M.D. Symes, L. Cronin, Decoupling hydrogen and oxygen evolution during electrolytic water splitting using an electron-coupled-proton buffer, *Nat. Chem.* 5 (2013) 403.
- L. Yang, G. Yu, X. Ai, et al., Efficient oxygen evolution electrocatalysis in acid by a perovskite with face-sharing IrO<sub>6</sub> octahedral dimers, *Nat. Commun.* 9 (2018) 5236.
- J. Suntivich, K.J. May, H.A. Gasteiger, J.B. Goodenough, Y. Shao-Horn, A perovskite oxide optimized for oxygen evolution catalysis from molecular orbital principles, *Science* 334 (2011) 1383–1385.
- L.C. Seitz, et al., A highly active and stable IrO<sub>x</sub>/SrIrO<sub>3</sub> catalyst for the oxygen evolution reaction, *Science* 353 (2016) 1011–1014.
- V. Georgakilas, J.A. Perman, J. Tucek, R. Zboril, Broad family of carbon nanoallotropes: classification, chemistry, and applications of fullerenes, carbon dots, nanotubes, graphene, nanodiamonds, and combined superstructures, *Chem. Rev.* 115 (2015) 4744–4822.
- S. Möller, et al., Online monitoring of electrochemical carbon corrosion in alkaline electrolytes by differential electrochemical mass spectrometry, *Angew. Chem. Int. Ed.* 59 (2020) 1585–1589.
- Y. Yi, et al., Electrochemical degradation of multiwall carbon nanotubes at high anodic potential for oxygen evolution in acidic media, *ChemElectroChem* 2 (2015) 1929–1937.
- B. Anasori, M.R. Lukatskaya, Y. Gogotsi, 2D metal carbides and nitrides (MXenes) for energy storage, *Nat. Rev. Mater.* 2 (2017) 16098.
- J. Zhang, Y. Zhao, X. Guo, et al., Single platinum atoms immobilized on an MXene as an efficient catalyst for the hydrogen evolution reaction, *Nat. Catal.* 1 (2018) 985–992.
- I.C. Man, et al., Universality in oxygen evolution electrocatalysis on oxide surfaces, *ChemCatChem* 3 (2011) 1159–1165.
- Umicore purchase price. <https://pmm.umicore.com/en/prices> (22/04/2022).
- H. Fei, et al., General synthesis and definitive structural identification of MN<sub>4</sub>C<sub>4</sub> single-atom catalysts with tunable electrocatalytic activities, *Nat. Catal.* 1 (2018) 63–72.
- A. Mehmood, M. Gong, F. Jaouen, et al., High loading of single atomic iron sites in Fe–NC oxygen reduction catalysts for proton exchange membrane fuel cells, *Nat. Catal.* 5 (2022) 311–323.
- D. Voiry, H. Shin, K. Loh, et al., Low-dimensional catalysts for hydrogen evolution and CO<sub>2</sub> reduction, *Nat. Rev. Chem.* 2 (2018) 0105.
- Y.R. Zheng, J. Vernieres, Z. Wang, et al., Monitoring oxygen production on mass-selected iridium–tantalum oxide electrocatalysts, *Nat. Energy* 7 (2022) 55–64.
- R.R. Rao, M.J. Kolb, L. Giordano, et al., Operando identification of site-dependent water oxidation activity on ruthenium dioxide single-crystal surfaces, *Nat. Catal.* 3 (2020) 516–525.
- D. Liu, X. Li, S. Chen, et al., Atomically dispersed platinum supported on curved carbon supports for efficient electrocatalytic hydrogen evolution, *Nat. Energy* 4 (2019) 512–518.
- J. Zhu, Y. Guo, F. Liu, et al., Regulative electronic states around ruthenium/ruthenium disulphide heterointerfaces for efficient water splitting in acidic media, *Angew. Chem., Int. Ed.* 133 (2021) 12436–12442.
- J.N. Tiwari, A.N. Singh, S. Sultan, K.S. Kim, Recent advancement of p- and d-block elements, single atoms, and graphene-based photoelectrochemical electrodes for water splitting, *Adv. Energy Mater.* 10 (2020) 2000280.
- C. Rong, X. Shen, Y. Wang, et al., Electronic structure engineering of single-atom Ru sites via Co–N<sub>4</sub> sites for bifunctional pH-universal water splitting, *Adv. Mater.* 34 (2022) 2110103.
- D. Wu, K. Kusada, S. Yoshioka, et al., Efficient overall water splitting in acid with anisotropic metal nanosheets, *Nat. Commun.* 12 (2021) 1145.
- L. Cao, Q. Luo, J. Chen, et al., Dynamic oxygen adsorption on single-atomic Ruthenium catalyst with high performance for acidic oxygen evolution reaction, *Nat. Commun.* 10 (2019) 4849.
- L. Shi, et al., Geometrically deformed iron-based single-atom catalysts for high-performance acidic proton exchange membrane fuel cells, *ACS Catal.* 12 (2022) 5397–5406.
- Q. Dang, H. Lin, Z. Fan, et al., Iridium metallene oxide for acidic oxygen evolution catalysis, *Nat. Commun.* 12 (2021) 6007.
- N. Li, L. Cai, C. Wang, Y. Lin, J. Huang, H. Sheng, H. Pan, W. Zhang, Q. Ji, H. I. Duan, et al., Identification of the active-layer structures for acidic oxygen evolution from 9R-BaIrO<sub>3</sub> electrocatalyst with enhanced iridium mass activity, *J. Am. Chem. Soc.* 143 (2021) 18001–18009.
- S. Laha, Y. Lee, F. Podjaski, D. Weber, V. Duppel, L.M. Schoop, F. Pielnhofer, C. Scheurer, K. Müller, U. Starke, K. Reuter, B.V. Lotsch, Ruthenium oxide nanosheets for enhanced oxygen evolution catalysis in acidic medium, *Adv. Energy Mater.* 9 (2019) 1803795.
- L. Cao, Q. Luo, J. Chen, L. Wang, Y. Lin, H. Wang, X. Liu, X. Shen, W. Zhang, W. Liu, Z. Qi, Z. Jiang, J. Yang, T. Yao, Dynamic oxygen adsorption on single-atomic Ruthenium catalyst with high performance for acidic oxygen evolution reaction, *Nat. Commun.* 10 (2019) 4849.
- H. Wang, J. Wu, A. Dolocan, Y. Li, X. Lü, N. Wu, K. Park, S. Xin, M. Lei, W. Yang, J. B. Goodenough, Short O–O separation in layered oxide Na<sub>0.67</sub>CoO<sub>2</sub> enables an ultrafast oxygen evolution reaction, *Proc. Natl. Acad. Sci. U.S.A.* 116 (2019) 23473–23479.
- P.S. Li, M.Y. Wang, X.X. Duan, L.R. Zheng, X.P. Cheng, Y.F. Zhang, Y. Kuang, Y. P. Li, Q. Ma, Z.X. Feng, W. Liu, X.M. Sun, Boosting oxygen evolution of single-atomic ruthenium through electronic coupling with cobalt-iron layered double hydroxides, *Nat. Commun.* 10 (2019) 1711.
- X. Mu, X. Gu, S. Dai, J. Chen, Y. Cui, Q. Chen, M. Yu, C. Chen, S. Liu, S. Mu, Breaking the symmetry of single-atom catalysts enables an extremely low energy barrier and high stability for large-current-density water splitting, *Energy Environ. Sci.* 15 (2022) 4048–4057.
- G. Kresse, J. Furthmüller, Efficient iterative schemes for ab initio total-energy calculations using a plane-wave basis set, *Phys. Rev. B* 54 (1996) 11169.
- J.P. Perdew, K. Burke, M. Ernzerhof, Generalized gradient approximation made simple, *Phys. Rev. Lett.* 77 (1996) 3865–3868.
- P.E. Blöchl, Projector augmented-wave method, *Phys. Rev. B: Condens. Matter Phys.* 50 (1994) 17953–17979.
- A. Tkatchenko, M. Scheffler, Accurate molecular van der Waals interactions from ground-state electron density and free-atom reference data, *Phys. Rev. Lett.* 102 (2009), 073005.
- K. Mathew, R. Sundaraman, K. Letchworth-Weaver, T. Arias, R.G. Hennig, Implicit solvation model for density-functional study of nanocrystal surfaces and reaction pathways, *J. Chem. Phys.* 140 (2014), 084106.



- [49] G.J. Martyna, M.L. Klein, M. Tuckerman, Nosé-Hoover chains: the canonical ensemble via continuous dynamics, *J. Chem. Phys.* 97 (1992) 2635–2643.
- [50] N. Saadatjou, A. Jafari, S. Sahebdehfar, Synthesis and characterization of Ru/Al<sub>2</sub>O<sub>3</sub> nanocatalyst for ammonia synthesis, *Iran. J. Chem. Chem. Eng.* 34 (2015) 1–9.
- [51] J.S. Luo, S. Yu, F. Fang, M. Lai, R. Sun, C.P. Wong, Investigating the mechanism of catalytic reduction of silver nitrate on the surface of barium titanate at room temperature: oxygen vacancies play a key role, *RSC Adv.* 5 (2015) 3377–3380.
- [52] J. Huang, Z. Jin, Z.-L. Xu, L. Qin, H. Huang, Z. Sadighi, S. Yao, J. Cui, B. Huang, J.-K. Kim, Porous RuO<sub>2</sub> nanosheet/CNT electrodes for DMSO-based Li-O<sub>2</sub> and Li ion O<sub>2</sub> batteries, *Energy Storage Mater.* 8 (2017) 110–118.
- [53] V. Pfeifer, T.E. Jones, J.J. Velasco Vélez, C. Massué, R. Arrigo, D. Teschner, F. Girgsdies, M. Scherzer, M.T. Greiner, J. Allan, M. Hashagen, G. Weinberg, S. Piccinin, M. Hävecker, A. Knop-Gericke, R. Schlögl, The electronic structure of iridium and its oxides, *Surf. Interface Anal.* 48 (2016) 261–273.
- [54] V. Pfeifer, T.E. Jones, J.J. Velasco Vélez, C. Massué, M.T. Greiner, R. Arrigo, D. Teschner, F. Girgsdies, M. Scherzer, J. Allan, M. Hashagen, G. Weinberg, S. Piccinin, M. Hävecker, A. Knop-Gericke, R. Schlögl, The electronic structure of iridium oxide electrodes active in water splitting, *Phys. Chem. Chem. Phys.* 18 (2016) 2292–2296.
- [55] F. Frati, M.O.J.Y. Hunault, F.M.F. De Groot, Oxygen K-edge X-ray absorption spectra, *Chem. Rev.* 120 (2020) 4056–4110.
- [56] S.K. Ojha, et al., Oxygen vacancy induced electronic structure modification of KTaO<sub>3</sub>, *Phys. Rev. B* 8 (2021), 085120.
- [57] K.M. Glassford, J.M. Chelikowsky, Electronic and structural properties of RuO<sub>2</sub>, *Phys. Rev. B* 47 (1993) 1732–1741.
- [58] S.P. Wu, H.M. Liu, Z. Huang, H.L. Xu, W. Shen, O-vacancy-rich porous MnO<sub>2</sub> nanosheets as highly efficient catalysts for propane catalytic oxidation, *Appl. Catal. B: Environ.* 312 (2022), 121387.
- [59] O. Marin-Flores, L. Scudiero, Su Ha, X-ray diffraction and photoelectron spectroscopy studies of MoO<sub>2</sub> as catalyst for the partial oxidation of isooctane, *Surf. Sci.* 603 (2009) 2327–2332.
- [60] K. Hagiwara, T. Ebihara, N. Urasato, T. Fujikawa, Application of <sup>129</sup>Xe NMR spectroscopy to analysis of CoMo/Al<sub>2</sub>O<sub>3</sub> hydrodesulfurization catalyst-effect of sulfidation on <sup>129</sup>Xe NMR spectra, *J. Jpn. Petrol. Inst.* 50 (2007) 139–146.
- [61] J. Halim, K.M. Cook, M. Naguib, P. Eklund, Y. Gogotsi, J. Rosen, M.W. Barsoum, X-ray photoelectron spectroscopy of select multi-layered transition metal carbides (MXenes), *Appl. Surf. Sci.* 362 (2016) 406–417.
- [62] K. Murugappan, E.M. Anderson, D. Teschner, et al., Operando NAP-XPS unveils differences in MoO<sub>3</sub> and Mo<sub>2</sub>C during hydrodeoxygenation, *Nat. Catal.* 1 (2018) 960–967.
- [63] Q. He, Y. Zhou, H. Shou, X. Wang, P. Zhang, W. Xu, S. Qiao, C. Wu, H. Liu, D. Liu, S. Chen, R. Long, Z. Qi, X. Wu, L. Song, Synergic reaction kinetics over adjacent ruthenium sites for superb hydrogen generation in alkaline media, *Adv. Mater.* 34 (2022) 2110604.
- [64] B. Ren, D. Li, Q. Jin, H. Cui, C. Wang, In-situ tailoring cobalt nickel molybdenum oxide components for overall water-splitting at high current densities, *ChemElectroChem* 6 (2019) 413–420.
- [65] X. Liu, S. Xi, H. Kim, et al., Restructuring highly electron-deficient metal-metal oxides for boosting stability in acidic oxygen evolution reaction, *Nat. Commun.* 12 (2021) 5676.
- [66] K. Qadir, S.H. Joo, B.S. Mun, D.R. Butcher, J.R. Renzas, F. Aksoy, Z. Liu, G. A. Somorjai, J.Y. Park, Intrinsic relation between catalytic activity of CO oxidation on Ru nanoparticles and Ru oxides uncovered with ambient pressure XPS, *Nano Lett.* 12 (2012) 5761–5768.
- [67] J. Kibsgaard, I. Chorkendorff, Considerations for the scaling-up of water splitting catalysts, *Nat. Energy* 4 (2019) 430–433.
- [68] A.R. Zeradjanin, J. Masa, I. Spanos, R. Schlögl, Activity and stability of oxides during oxygen evolution reaction-from mechanistic controversies toward relevant electrocatalytic descriptors, *Front. Energy Res.* 8 (2021), 613092.
- [69] M. Retuerto, L. Pascual, F. Calle-Vallejo, P. Ferrer, D. Gianolio, A.G. Pereira, Á. García, J. Torrero, M.T. Fernández-Díaz, P. Bencok, M.A. Peña, J.L.G. Fierro, S. Rojas, Na-doped ruthenium perovskite electrocatalysts with improved oxygen evolution activity and durability in acidic media, *Nat. Commun.* 10 (2019) 2041.
- [70] L. Zhang, H. Jang, H. Liu, M.G. Kim, D. Yang, S. Liu, X. Liu, J. Cho, Sodium-decorated amorphous/crystalline RuO<sub>2</sub> with rich oxygen vacancies: a robust pH-universal oxygen evolution electrocatalyst, *Angew. Chem. Int. Ed.* 60 (2021) 18821–18829.
- [71] R. Anand, A.S. Nissimagoudar, M. Umer, et al., Late transition metal doped MXenes showing superb bifunctional electrocatalytic activities for water splitting via distinctive mechanistic pathways, *Adv. Energy Mater.* 11 (2021) 2102388.
- [72] M. Umer, S. Umer, M. Zafari, et al., Machine learning assisted high-throughput screening of transition metal single atom based superb hydrogen evolution electrocatalysts, *J. Mater. Chem. A* 10 (2022) 6679–6689.
- [73] A. Li, S. Kong, C. Guo, et al., Enhancing the stability of cobalt spinel oxide towards sustainable oxygen evolution in acid, *Nat. Catal.* 5 (2022) 109–118.